

On the Microstructural and Cyclic Mechanical Properties of Pure Iron Processed by Electron Beam Melting

Christof Johannes Jaime Torrent,* Steffen Wackenrohr, Julia Richter, César Ernesto Sobrero, Sebastian Degener, Philipp Krooß, Hans Jürgen Maier, and Thomas Niendorf

Additive manufacturing (AM) processes such as electron beam melting (EBM) are characterized by unprecedented design freedom. Topology optimization and design of the microstructure of metallic materials are enabled by rapid progress in this field. The latter is of highest importance as many applications demand appropriate mechanical as well as functional material properties. For instance, biodegradable implants have to meet mechanical properties of human bone and at the same time guarantee adequate cytocompatibility and degradation rate. In this field, pure iron has come into focus in recent studies due to its low toxicity. Hierarchical microstructures resulting from the EBM solidification processes and intrinsic heat treatment, respectively, allow for an adjustment of the degradation behavior and may promote enhanced fatigue strength. Herein, commercially pure iron (cp-Fe) is processed by EBM. Microstructural analysis as well as an evaluation of the cyclic mechanical material properties are conducted. The results are compared to a hot-rolled (HR) reference material. A contradiction observed as the EBM-processed cp-Fe (EBM Fe) shows lower ultimate tensile strength under monotonic loading but improved fatigue properties compared to the HR Fe. It is revealed that such a unique behavior originates from prevailing microstructural features in the EBM as-built condition.

1. Introduction


Additive manufacturing (AM) can not only be exploited for significant improvement with respect to design freedom, which, in particular, is of the highest interest in industrial fields, where specific parts in low numbers are demanded, for example, implant surgery,^[1] but also be used for direct microstructure design and, thus, tailoring of local functional properties. For example, AM can be used for manufacturing of parts featuring defect-tolerant microstructures^[2] or labeling of parts by microstructural gradation.^[3] Numerous studies have been conducted to directly design a process/material-specific microstructure since the mechanical behavior and isotropy of a component highly depend on microstructural features, such as grain size and grain orientation. The feasibility of processing of ready-to-use complex objects without the necessity of tooling and heat treatment is one of the major topics of numerous recent studies focusing on AM.^[4–7]

In the field of medical applications, several crucial issues need to be addressed. For instance, the toxicity or biocompatibility of the selected materials^[8] as well as tissue generation on the implant surface has to be taken into account.^[1,9–11] In many cases a rather low modulus of elasticity is favorable to counteract stress shielding and, thus, possible bone resorption, which is known to lead to severe complications after a surgical intervention.^[1,8,12] Thus, the adaption of Young's modulus and yield strength to match the mechanical properties of the bone is of crucial importance. In addition, the sufficient fatigue strength of AM implants over their entire lifetime is an indispensable necessity as loading cycles can be up to millions per year.^[13,14] Therefore, high fatigue strength is needed for a successful application of implant materials.

Due to superior cost efficiency (compared to most conventional implant materials in the medical sector, e.g., titanium alloys, ceramics), commercially pure iron (cp-Fe) has received significant attention in recent years. Implant surgery nowadays focuses on the application of biodegradable materials, cp-Fe being a candidate material in this regard. However, only a few studies have focused on this topic.^[15–18] Initially, Fe was investigated in several studies focusing on novel biodegradable

C. J. J. Torrent, J. Richter, Dr. C. E. Sobrero, S. Degener, Dr. P. Krooß, Prof. T. Niendorf
Institute of Materials Engineering
University of Kassel
Kassel 34125, Germany
E-mail: torrent@uni-kassel.de

S. Wackenrohr, Prof. H. J. Maier
Institut für Werkstoffkunde (Materials Science)
Leibniz Universität Hannover
Garbsen 30823, Germany

 The ORCID identification number(s) for the author(s) of this article can be found under <https://doi.org/10.1002/adem.202100018>.

© 2021 The Authors. Advanced Engineering Materials published by Wiley-VCH GmbH. This is an open access article under the terms of the Creative Commons Attribution-NonCommercial-NoDerivs License, which permits use and distribution in any medium, provided the original work is properly cited, the use is non-commercial and no modifications or adaptations are made.

DOI: 10.1002/adem.202100018

stents^[19,20] already in the 2000s. Later, investigations on bone-stabilizing pins were conducted,^[21] revealing that cp-Fe shows no toxicity and, therefore, could be used as a promising candidate material for biodegradable implants. Nevertheless, higher degradation rates are desirable for most applications. In this regard, Kraus et al.^[21] attributed the sluggish degradation to a low oxygen content (being locally affected in dependence on the tissue) as well as a hampered oxygen transport due to adherent degradation products on the implant surface.

In their investigations on Fe processed by direct metal printing (DMP), Li et al.^[15] reported on the good mechanical properties as well as high cytocompatibility of cp-Fe and, thus, concluded on its promising potential in medical applications. Apart from the potential of application-oriented geometry customization, they also highlighted the possibility to manipulate the degradation behavior by adjusting the topology of the DMP-processed parts. However, in case of many envisaged applications, design freedom and topology customization are strongly restricted since geometrical constraints are mainly dominated by the specific application. In this regard, direct design of the mechanical properties and the biodegradation behavior by appropriate design of microstructural features using the intrinsic advantages of AM is seen to be very promising.

Lejček et al.^[22] processed cp-Fe via selective laser melting (SLM) as a model material and reported on hierarchical structures consisting of subgrains and cells resulting from multiple $\alpha \leftrightarrow \gamma$ phase transformations during AM processing. Song et al.^[23] correlated the applied SLM process parameters to the microstructure as well as dislocation density of cp-Fe and proposed a method to tailor the ultimate tensile strength. SLM mostly comprises a comparably low build plate temperature eventually promoting the formation of pronounced residual stresses upon processing. Furthermore, SLM is characterized by a high probability of picking up light elements during processing due to the actual process environment (shielding gas). Both shortcomings finally have a significant effect on the mechanical behavior. As powder bed processes using an electron beam as the energy source, that is, the electron beam melting (EBM) process, are characterized by high process temperatures under vacuum atmosphere, residual stresses and pickup of light elements, respectively, are strongly impeded. To the authors' best knowledge, cp-Fe has only been EBM-processed by Murr et al.^[24] so far. Applying bright-field transmission electron microscopy (TEM), a microstructure with a high density of nanoscaled dislocation substructures was revealed and rationalized based on the presence of δ -ferrite embedded in the α matrix (in defined crystallographic orientations).

To reveal the full potential of pure Fe for medical applications, cp-Fe was processed using EBM in the present study. The microstructural evolution as well as the properties under monotonic/quasistatic and cyclic mechanical loading were investigated and compared to hot-rolled pure Fe.

2. Experimental Section

Hot-rolled cp-Fe was used as ingot material for powder production using electron induction gas atomization (EIGA) by TLS (TLS Technik GmbH, Bitterfeld, Germany). Afterward,

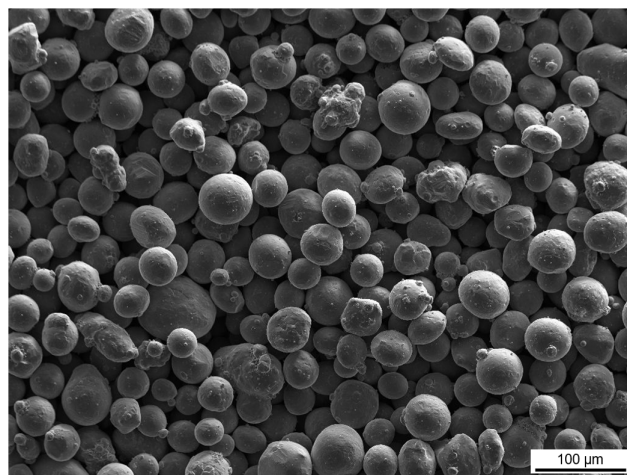


Figure 1. SEM micrograph of the cp-Fe powder.

the powder fraction ranging from 63 to 150 μm was processed in an Arcam A2X EBM machine (ARCAM AB, Mölndal, Sweden). As shown in **Figure 1**, the powder particles are spherical in general; however, a minor fraction of satellites is present. Before processing, the built plate was first heated to a nominal temperature of 400 $^{\circ}\text{C}$ for 10 min, resulting in a starting temperature of 500 $^{\circ}\text{C}$ below the build platform. The powder was spread in layers of 50 μm thickness (As the rake system used in ARCAM A2X EBM machines is a flexible metal comb, it is possible to deposit coarse particles eventually larger than the final layer thickness. This is not detrimental to the process since the space filling of the molten material is much higher than of the loose powder. This leads to the fact that the thickness of the deposited layer is higher compared to the nominal layer thickness, which in turn compensates for the loss of layer height after melting.) and subsequently preheated with 15 mA at an electron beam deflection speed of 12 000 mm s^{-1} for 12 repetitions, before being selectively melted with a beam current of 12.25 mA at a speed of 4000 mm s^{-1} using a hatch distance of 0.08 mm. Applying these parameters, a volume energy of 46 J mm^{-3} was applied to melt the cp-Fe powder during processing. The electron beam followed a meandering scanning strategy, rotated by 90 $^{\circ}$ after each layer. For microstructural characterization, small cubes of 10 \times 10 \times 10 mm^3 were manufactured, whereas tensile and fatigue samples were cut out of bars (13 mm in diameter, 60 mm in height) and tested in the as-built condition.

The chemical composition of both the initial HR material and the atomized and subsequently processed material was analyzed by means of X-ray fluorescence analysis for metallic elements, carrier gas hot extraction for the elements hydrogen, nitrogen, and oxygen, and combustion analysis for carbon and sulfur. Chemical analysis was performed by Revierlabor GmbH (Essen, Germany).

For microstructural investigations, 1 mm of the sample was first ground off to remove surface effects and then vibropolished to 0.04 μm using a colloidal suspension. Microstructural investigations were conducted employing scanning electron microscopy (SEM, Zeiss Ultra Plus). The scanning electron microscope was operated at a nominal voltage of 20 kV and

equipped with a back-scattered electrons (BSE) and an electron backscatter diffraction (EBSD) detector for grain orientation analysis. For all EBSD measurements the surfaces were electrolytically polished. EBSD micrographs were obtained using TSL OIM software (Version 7), and grain sizes were examined using the line intercept method.

To characterize the pore distribution and density, X-ray microcomputed tomography (μ -CT) was performed using a Zeiss Xradia Versa 520 operating at an acceleration voltage of 140 kV and a power of 10 mA. The probed volume was 6.5 mm³ considering a voxel size of 1.85 μ m³. The data obtained were reconstructed using Avizo 9.4 software. Due to the voxel size and data handling, analysis of pores with size less than 4 μ m was not reliable and, thus, not taken into account in the remainder of this work.

For X-ray diffraction and pole figure measurements, respectively, samples were polished down to P4000 grit and then vibropolished. A Seifert XRD 3003 Micro X-ray diffractometer using a cobalt K α source, operated at 40 kV and 35 mA, equipped with a monochromator and a 5 mm polycapillary collimator was used for data acquisition. Pole figures from the three main peaks (110), (200), and (211) were experimentally determined. The orientation distribution function (ODF) was calculated using the MTEX package.^[25]

To analyze the phase evolution in a larger sample volume, high-energy X-ray diffraction (HE-XRD) experiments were performed at P07 PETRA III at DESY (Hamburg, Germany).^[26] A primary beam of 87.1 keV (0.0142347 nm) and a Perkin Elmer XRD 1621 Flat Panel detector were used. A total of 20 measurements were conducted, each at an exposure time of 0.1 s.

To characterize the mechanical properties of the HR- and EBM-processed material conditions, hardness was determined by automated microindentation testing using a Struers DuraScan 70 applying a load of 9.8 N (HV1) for 10 s at 21 measurement points per sample. Tensile tests were conducted considering four samples in each case (nominal cross sections of 1.5 \times 3 mm²) using an MTS Criterion Model 43 operated in displacement control applying a crosshead displacement rate of 2 mm min⁻¹. The actual gage section dimensions were determined for every sample and used for calculation of stresses. The elongation was measured up to 30 % strain via an extensometer (gauge length of 5 mm) directly attached to the sample surface. Above 30 %, the strain was calculated based on the displacement signal. All the samples were machined by electrical discharge machining (EDM) and ground to a surface roughness of 5 μ m. For all samples, the loading direction was aligned parallel to the build direction (BD).

For high cycle fatigue (HCF) testing, samples were designed according to DIN 50113 and electrolytically polished down to a surface roughness of around 0.06 μ m to minimize the influence of surface notches. Testing was done under three-point rotating-bending-loading. The fatigue tests were conducted on a Zwick/Roell UBM 200tC rotating-bending machine. The samples were fatigued under force control with various stress amplitudes ($\Delta\sigma/2$) ranging from 200 to 400 MPa at a bending load ratio of $R = -1$. The rotational speed in the test was always set to 1000 min⁻¹. The stress amplitude at the edge layer was calculated according to $\Delta\sigma/2 = 32M/(\pi d^3)$, where M represents the bending moment and d the sample diameter in the measuring range after electropolishing.

3. Results and Discussion

3.1. Microstructure

Table 1 shows the chemical composition of the cp-Fe in the HR condition as well as after gas atomization and subsequent processing by EBM. Only a minor fraction of impurities is found and, thus, both material conditions can be referred to as commercially pure. Lower contents of the elements oxygen and nitrogen were determined after EBM processing. This decrease in light elements is attributed to the process conditions prevailing during EBM, most importantly the vacuum environment needed for robust processing. In previous studies, the evaporation of heavier elements has already been observed, for example, Mn in case of processing of high-Mn steels by EBM.^[2,27] In case of Mn, the reason is seen in the very low vapor pressure of the element. In line with this argumentation, the evaporation of light elements is thought to be reasonable as long as these elements are not bound in the form of very stable modifications. However, it has to be emphasized at this point that an uncontrolled element evaporation is not favorable in most cases because the nominal and the local alloy composition can deviate, leading to locally different properties. In terms of the findings presented here and the base metal considered, that is, cp-Fe, detrimental effects are not expected.

To assess the porosity of the EBM-processed condition, μ -CT analysis was performed. Figure 2 shows the μ -CT measurement (a), the calculated pore volume (b), and the sphericity of pores

Table 1. Chemical composition of hot-rolled and EBM-processed cp-Fe.

Element	HR Fe [wt%]	EBM-processed cp-Fe [wt%]
Al	0.008	0.005
Co	<0.01	<0.01
Cr	<0.01	<0.01
Cu	<0.01	0.01
Fe	Basis	Basis
Mn	0.03	0.03
Mo	<0.01	<0.01
Nb	<0.01	<0.01
Ni	<0.01	0.01
P	<0.005	<0.005
Pb	<0.02	<0.02
Si	<0.01	<0.01
Sn	<0.01	<0.01
Ta	<0.02	<0.02
Ti	<0.01	<0.01
V	<0.01	<0.01
W	<0.02	<0.02
Zn	<0.01	<0.01
O	0.0166	0.0059
N	0.005	<0.002
C	<0.005	<0.005
S	0.002	0.003

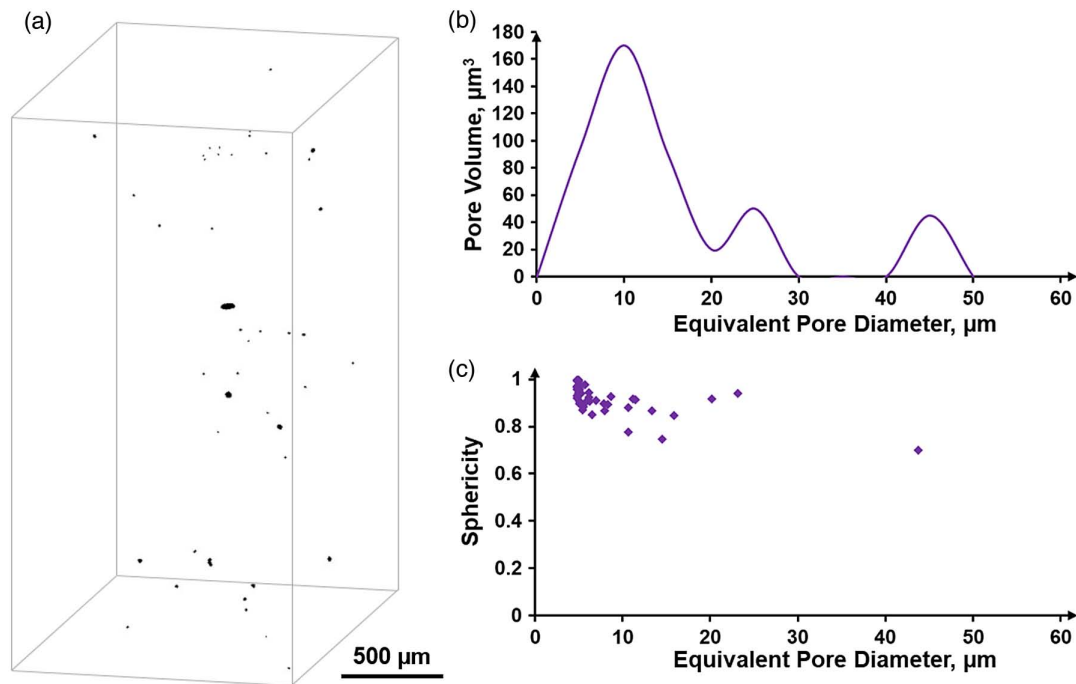


Figure 2. a) Defect distribution within a representative volume of the EBM-processed cp-Fe analyzed by μ -CT, b) calculated pore volumes, and c) sphericity of pores versus equivalent pore diameter.

plotted versus the equivalent pore diameter (c). Based on the data obtained, the material is characterized by a density of $>99.99\%$. A uniform distribution of the pores throughout the EBM-processed cp-Fe is evident. The dominant volume fraction of pores is characterized by a diameter below $20\ \mu\text{m}$; the calculated average pore diameter is $\approx 8\ \mu\text{m}$. Only one pore with a size of $45\ \mu\text{m}$ could be detected in this representative sample volume. The average sphericity of the pores is 0.92 , clearly being very close to a perfectly spherical shape. The coincidence of small pore diameters and the high sphericity clearly indicate gas entrapment in the feedstock powder as the reason for pore formation.^[28–30] Thus, lack of fusion porosity as well as keyholing effects could be avoided in the process parameter window elaborated within the parameter study conducted.

In the further course of the present paper, *grains* are defined by being separated from each other by grain boundaries with a misorientation angle of more than 15° .^[31] These are referred to as *high-angle grain boundaries (HAGB)*. Structures with a misorientation of less than 15° are referred to as *subgrains* and are separated by *low-angle grain boundaries (LAGBs)*.^[32] The specific role of the different boundary nature and its contribution to the strength in different loading conditions will be discussed in more detail in the remainder of this work.

As can be deduced from **Figure 3a,b**, the microstructure of the EBM-processed cp-Fe features a complex grain morphology characterized by severe grain fragmentation, as highlighted by the dotted lines in **Figure 3a**. The grains are slightly elongated along BD, whereas the HR reference material shows a more homogeneous and equiaxed grain morphology without any preferred elongation direction or any visible substructures (**Figure 3c**). Similar observations were also made in HR and

annealed Fe bars by Bruder^[33] and Muñoz et al.^[34] The average grain aspect ratio for the EBM-processed cp-Fe is below 0.5 .

An irregular grain morphology similar to that of the EBM-processed cp-Fe presented herein was already reported for Fe after SLM. In studies published by Lejček et al.^[22] and Song et al.,^[23] this kind of final microstructural appearance was rationalized based on multiple $\alpha \leftrightarrow \gamma$ phase transformations, which in turn led to a fragmentation of priorly columnar solidified grains. Furthermore, the high dislocation density found in these studies was attributed to thermal contraction resulting from high cooling rates, leading in turn to work hardening of the material. Another mechanism concerning a complex solidification history was reported by Günther et al.^[2] in a study focusing on EBM-processed Cr–Mn–Ni steel. Multiple phase transformations stimulated by the intrinsic heat treatment being characteristic for AM processing were found to promote significant grain refinement and eventually evolution of an isotropic microstructure. Here, EBSD measurements were performed to get a more detailed insight into the boundary arrangements.

From the inverse pole figure (IPF) maps in **Figure 4a,b**, the aforementioned deviations in local contrasts can be identified as a high volume fraction of subgrains within the grains. HAGBs are marked by continuous lines, and the subgrains are marked by dotted lines highlighting the LAGB character. In **Figure 5**, the misorientation angle distributions of the two compared material conditions are displayed. In the EBM-processed cp-Fe, a high number fraction of the boundaries are of a low-angle character, whereas in the microstructure in the HR Fe the majority of grain boundaries can be characterized as HAGBs.

According to the aforementioned studies,^[2,22,23] a tendency to grain fragmentation can be seen in case of AM processing

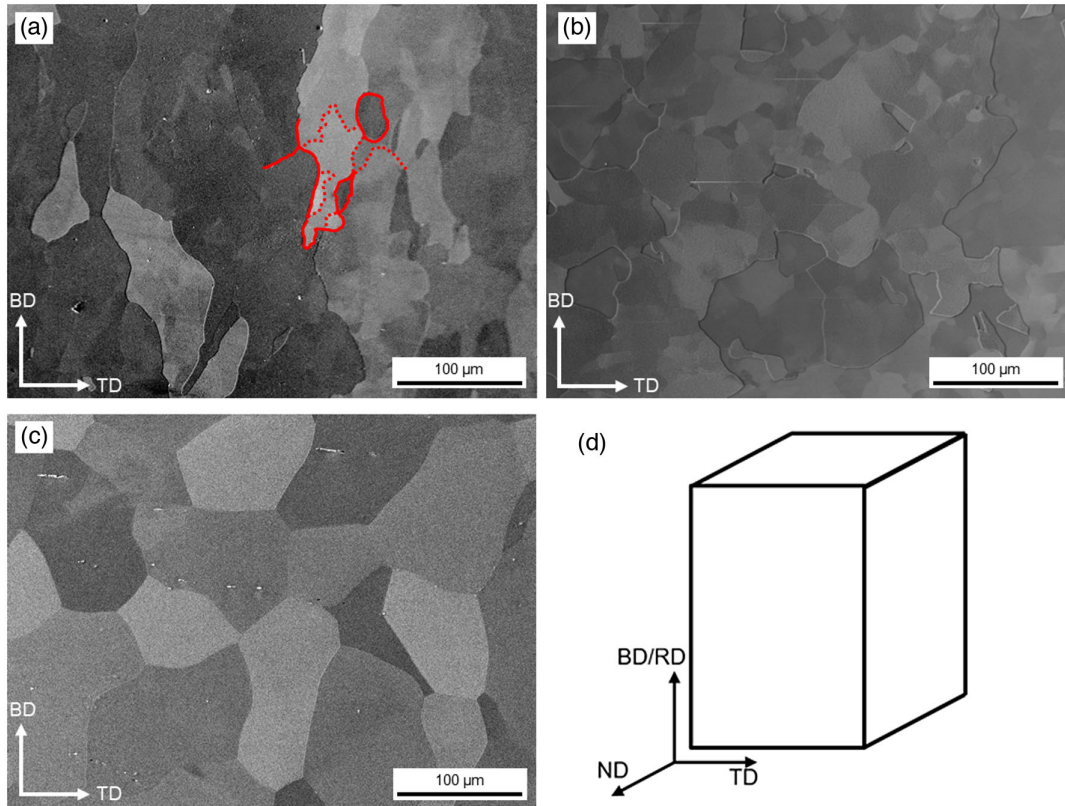


Figure 3. Back-scattered electrons micrographs of a) EBM-processed cp-Fe in side view and b) in top view and c) HR Fe in side view; d) schematic defining the relevant directions.

of Fe-based alloys. In these studies it is considered that grain refinement stems from the intrinsic heat treatment being characteristic of any AM process. In contrast to an HR process, where high mechanical stresses providing the driving force for recrystallization are present, the EBM process is known to be hardly affected by such stresses due to its high process temperature. Apart from this, a grain refinement can also proceed as a consequence of repeated allotropic phase transformations. As stated in Lejček et al.,^[22] previously columnar grains can disaggregate in consequence of repeated phase transformations: First, an epitaxial solidification in the melt pool (at the bottom) enforces a columnar grain growth due to the selection of preferred orientations aligned to the temperature gradient. Thereby, as a result of extremely high cooling rates prevailing directly upon solidification, α phase grains are formed directly. In the further course of repeated intrinsic reheating, volume changes resulting from $\alpha \leftrightarrow \gamma$ transitions lead to inter- and intragranular stresses. Mechanisms known as autocatalytic nucleation of new grains^[35] and elastic-plastic accommodation^[36] are mechanisms to accommodate these stresses, and as a consequence, grain refinement can result. However, if the general process temperature level is not in the region of phase transformation ($\alpha \leftrightarrow \gamma$ at 911 °C in iron), distinctly less transformation events occur. Furthermore, the driving force necessary for grain refinement is low. The EBM-specific high process temperature facilitates recovery, that is, a reduction of stresses through the rearrangement of prevailing dislocations. In consequence, the formation

of a high fraction of subgrain structures rather than high-angle borders leads to the final appearance of the as-built microstructure shown in Figure 4.

Apart from the number of phase transformations, the factors that have an influence on the final microstructure are manifold. Process-specific thermal histories and material characteristics are input variables, and the local temperature gradients, the homologous temperatures in the direct vicinity of the melt pool, as well as the melt viscosity and turbulences are not yet known. The contributing mechanisms and their individual impact are not trivial, and thus, beyond the scope of the current study.

Taking into account that grains are separated by HAGBs only, the EBM-processed cp-Fe can be referred to as coarse-grained (200 μm), whereas the grains of the HR Fe are almost four times smaller (62 μm). These differences in absolute grain sizes have to be evaluated carefully. Figure 4 clearly reveals that the EBM process leads to the formation of small subgrains. The complex origin of these structures has been discussed before. The extent to which these LAGBs contribute to the overall mechanical behavior is discussed in the second part of this section.

Pole figures obtained by XRD are shown in Figure 6a. Evolution of a pronounced texture can be seen, eventually being characterized by a maximum value of *multiples of random distribution* (m.r.d.) of 14. As the built geometry is a cube, scan tracks always passed alongside (in transverse direction (TD)) or orthogonal to the analyzed surface, which is normal direction (ND). As a consequence, a preferred orientation of the crystallites is seen

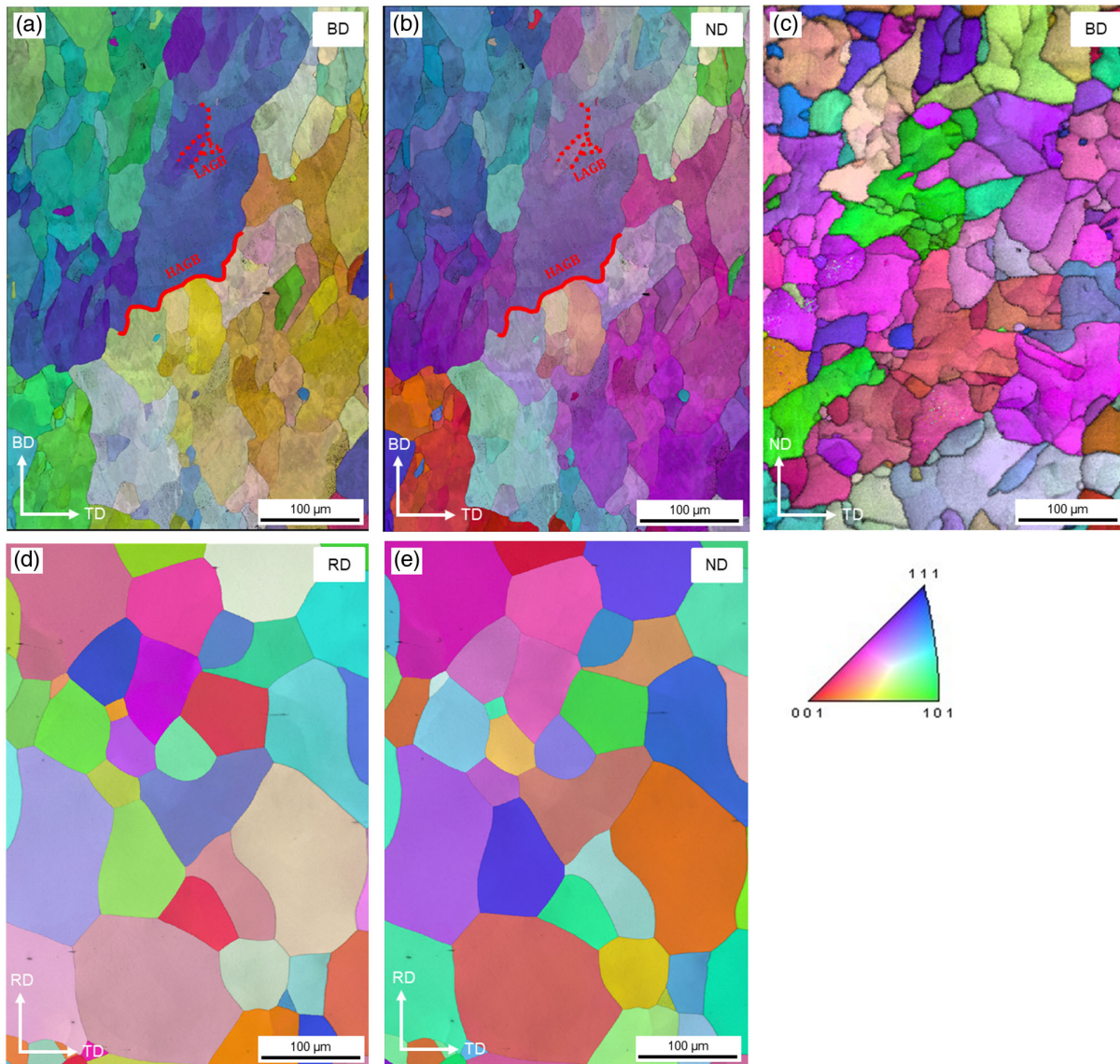


Figure 4. EBSD analysis (inverse pole figure maps): a) EBM-processed cp-Fe in side view plotted with respect to BD and b) normal direction; c) top view indexed with respect to BD. d, e) HR Fe plotted with respect to (d) rolling direction and (e) normal direction.

aligned to the scanning direction. However, no tilting around the BD axis is observed. In every process related to metal solidification, the major impact factors related to grain growth, grain morphology, and grain orientation are the solidification speed (v) and the direction of the thermal gradient (G) in the melt pool. Considering a preferred solidification in $\langle 001 \rangle$ direction parallel to the thermal gradient for cubic systems,^[37] one can deduce a gradient strongly oriented alongside the scan track in case of the parameters applied. In a study focusing on grain structure evolution in IN 718, Helmer et al.^[6] could demonstrate a high impact of the scanning parameters on the local heat flow. Increasing the beam speed at a constant volume energy resulted in a change in the direction of the local temperature gradient, which in turn led to an impeded columnar grain growth. As a result, a strongly reduced degree of grain elongation alongside BD and an

enforced texture in dependence of the scanning direction was found. This phenomenon is also visible in the EBM-processed cp-Fe presented herein.

For a different view, an inverse pole figure, measured on the same surface, is added in Figure 6b, where a significant texture with most of the (001) planes being oriented in normal direction (ND) and no significant texture intensity parallel to the BD can be seen. This result is in accordance with the pole figure calculated from EBSD data (not shown). Thus, the macro (XRD) and micro (EBSD) texture coincide. At this point it is important to note that the EBSD measurement at the applied magnification (cf., Figure 4) covers only a few grains and therefore does not represent a global texture.

The texture development is different from many other alloys processed by EBM. Especially alloys characterized by the absence

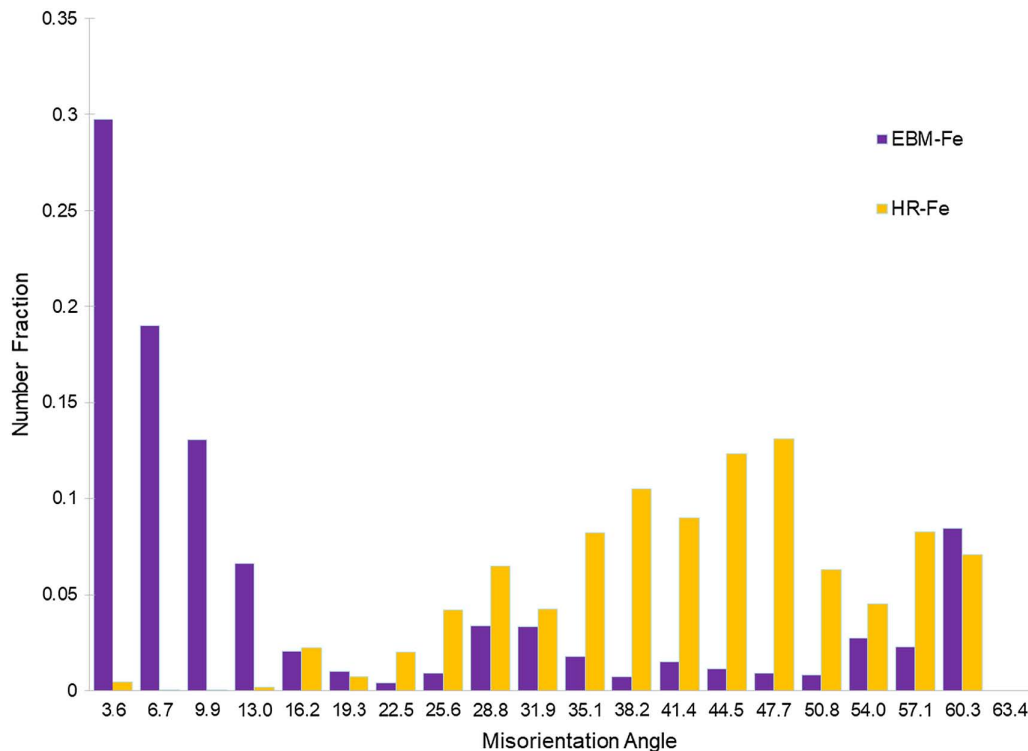


Figure 5. Misorientation angle distribution for EBM-processed cp-Fe and HR Fe.

of a phase transformation upon solidification, for example, austenitic stainless steel AISI 316L, tend to develop a microstructure characterized by preferred $\langle 0\ 0\ 1 \rangle$ orientation alongside BD featuring a very low aspect ratio (columnar grains). Precise manipulation of the texture and grain morphology by adjusting the aforementioned influencing factors (solidification speed and thermal gradient) is subject of many research efforts reported for the EBM process^[6,7,38,39] as well as for the SLM process.^[3] However, cp-Fe has rarely been processed via EBM until now.^[24] The potential to tailor the microstructure and, thus, the mechanical properties directly upon processing has to be analyzed in future studies.

Figure 7 shows an intensity plot obtained by integrating HE-XRD measurements. As can be seen at the first glance, only planes being related to the α -ferritic structure are shown and no retained nonequilibrium δ -ferrite is detected, as was previously reported by Murr et al.^[24] In their publication, this metastable phase was found in the powder used as well as after EBM processing. The appearance of a pronounced yield point was attributed to this phenomenon. Obviously, the initial condition of the powder, including the impurity level, processing conditions, and many other factors, contributes to the overall solidification path. However, the differences seen cannot be evaluated based on the data available and future studies are needed at this point.

3.2. Mechanical Properties

The stress–strain curves for both material conditions, that is, HR FE and EBM-processed cp-Fe, shown in **Figure 8** reveal a ductile

behavior in both cases characterized by almost equal strains at fracture of more than 60%. The yield strength of the EBM-processed cp-Fe is slightly higher compared to the HR Fe (210 and 193 MPa, respectively). Both stress–strain curves show a pronounced yield point, probably stemming from interstitial atoms inside the matrix (see Table 1), eventually promoting dislocation pinning and strain aging, respectively. Thus, the slightly lower content of those elements in the EBM-processed cp-Fe after processing could be responsible for the differences seen in terms of the initial yielding behavior. The higher yield strength (in terms of the absolute value) of the EBM-processed cp-Fe is in line with the hardness measurement results, which are 83.6 HV1 for the EBM-processed cp-Fe and 67.9 HV1 for the HR Fe. This difference in turn indicates that, despite the generally coarser grain structure (taking into account the HAGBs only), the high density of LAGBs significantly contributes to the strength and the Hall-Petch effect,^[31] respectively. According to Niendorf et al.,^[40] in the LCF regime interactions between dislocations and LAGBs can lead to a rearrangement of the latter, and thus, to cyclic softening. Nonetheless, in quasi-static loading a high fraction of LAGBs can have a strong impact on dislocation movement, which is reflected in the higher yield strength of the EBM-processed cp-Fe compared to the HR Fe. Further, Bruder^[33] pointed out that a high proportion of LAGBs in cp-Fe has no negative influence on the fatigue strength in HCF testing. By direct comparison of the two curves, a stronger increase in stress after the Lüders strain can be seen in the HR-Fe reference condition, probably stemming from a lower dislocation density in the non-deformed condition eventually allowing for a higher rate of work hardening. For the EBM-processed cp-Fe and HR Fe ultimate

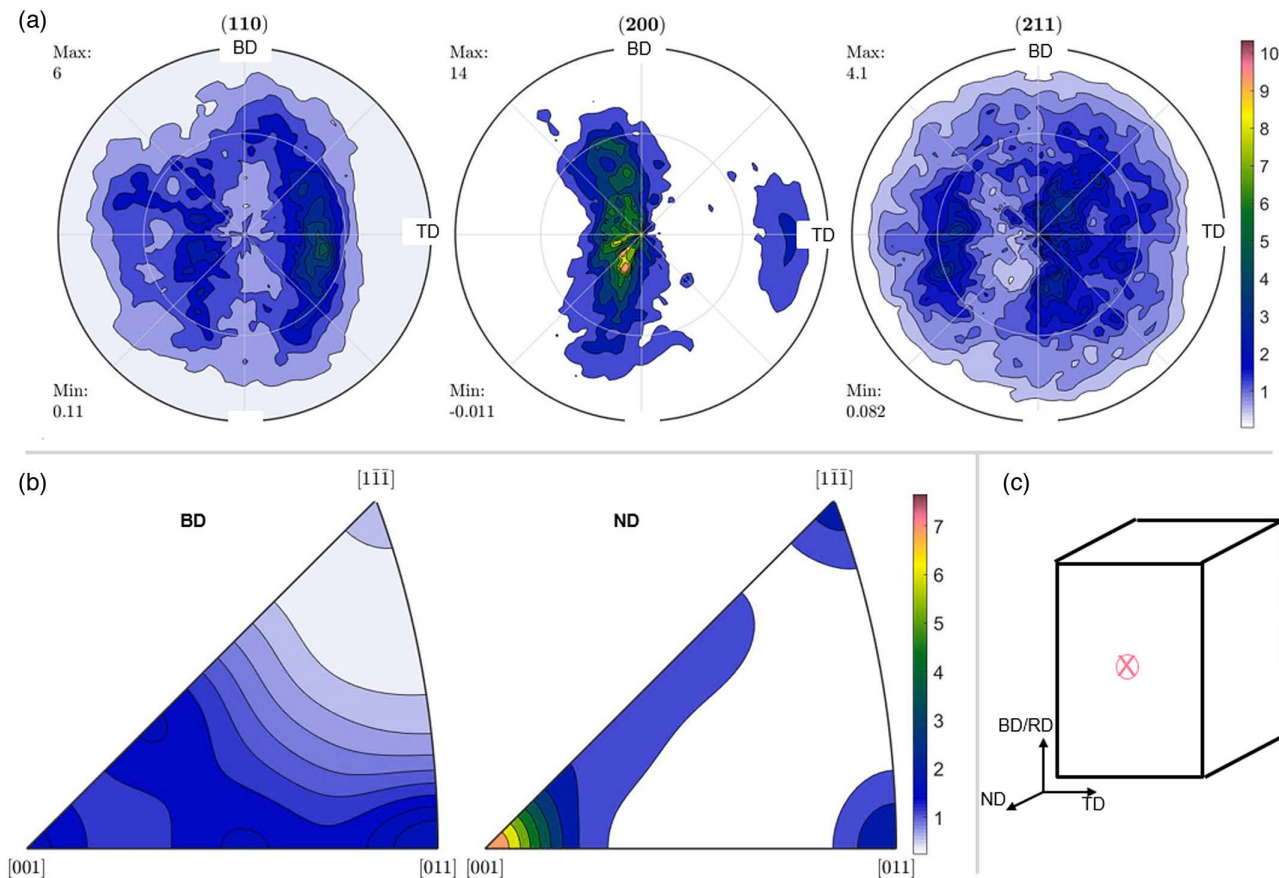


Figure 6. a) Pole figures for EBM-processed cp-Fe; b) inverse pole figures calculated for the same surface; c) schematic indicating the probed spot by the red “X.”

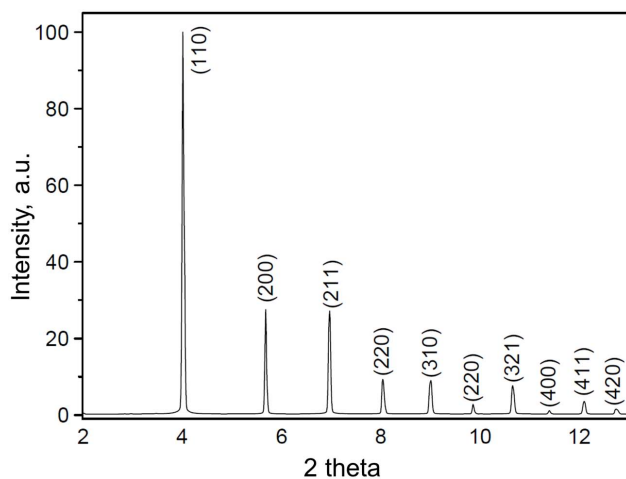


Figure 7. Diffraction pattern of an EBM-processed cp-Fe obtained by HE-XRD at the PETRA III synchrotron source.

tensile strengths of 248 and 267 MPa, respectively, could be identified. Due to the pronounced ductility of the cp-Fe in both conditions, pores not detected by means of μ -CT are not expected to be damage-relevant in the analyzed specimens.

The $S-N$ curves for EBM-processed cp-Fe and for HR Fe are shown in **Figure 9**. Due to the stress calculation based on the bending moment with the assumption of a linear-elastic material behavior, the stresses in the fatigue tests are clearly overestimated, eventually exceeding the actual tensile strength of the material. These stresses only occur in the surface area of the samples and are reduced at the beginning of the test by plastic flow. As a reference, fatigue test data for an HR condition reported by Bruder^[33] are also plotted in Figure 9. The EBM-processed cp-Fe shows a clearly higher fatigue strength than the HR condition, and the stress amplitudes are increased by 70 MPa on average. The fatigue strength, determined at $N = 5 \times 10^6$ for both material states, was found to be 225 MPa for the HR Fe and 325 MPa for the EBM-processed cp-Fe. The excellent fatigue behavior of the EBM-processed cp-Fe in the HCF range could result from the very low fraction of pores and other defects, as could be confirmed by μ -CT analysis. Usually, HCF properties are dominated by the presence of such defects,^[41] especially if they appear in the direct vicinity of the sample surface.^[42] In Figure 2, it was shown that the porosity is mainly a result of gas entrapment leading to the formation of small pores with high sphericity. Spherical pores with a small diameter are less likely to act as notches and crack-initiating features in the microstructure. Furthermore, the superior fatigue performance can be attributed

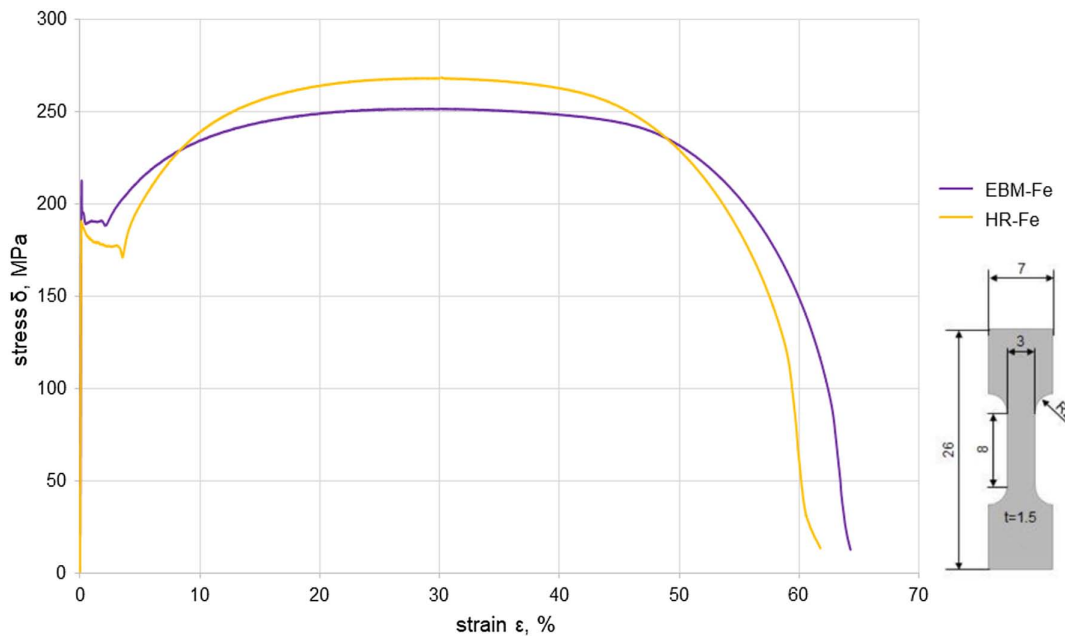


Figure 8. Stress–strain curves of HR Fe and EBM-processed cp-Fe as well as details on sample geometry and dimensions shown on the right (all values in millimeter).

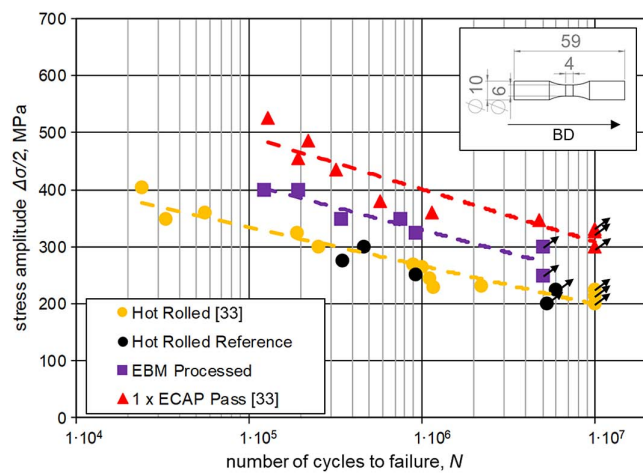


Figure 9. S–N fatigue curves (bending fatigue) for the HR Fe and EBM-processed cp-Fe. For reference data from the literature are shown highlighting the fatigue properties of Fe featuring similar microstructures.

to the differing microstructures, that is, the high fraction of LAGBs in the EBM-processed cp-Fe (Figure 4). Similar microstructural features have been reported in studies focusing on ultrafine-grained (UFG) materials obtained by equal channel angular pressing (ECAP). Induced by repeated severe shear deformation, grain refinement is promoted to a submicron level during ECAP, eventually having a positive effect on the fatigue life (most effectively in the HCF regime).^[33,43] The S–N curve for cp-Fe after one ECAP pass was elaborated by Bruder.^[33] This curve is also shown for reference in Figure 7. The stress amplitudes are on average 150 MPa higher (at the

same number of cycles to failure) compared to the HR state and, thus, also well above the EBM-processed cp-Fe. In case of ECAP-processed material, the increased fatigue strength can be also rationalized based on a high fraction of LAGBs.

In studies of Niendorf et al.,^[32,40,44–48] the low-cycle-fatigue (LCF) behavior of ECAP-processed UFG interstitial-free (IF) steels (consisting of 99.85% Fe) was investigated. These studies focused on the nature of HAGBs as well as LAGBs and their influence on the fatigue performance.^[40,45,48] It was shown that an UFG microstructure containing a high density of HAGBs is characterized by superior fatigue strength in the LCF regime. This was attributed to the effectively inhibited dislocation movement. Under given loading conditions, LAGB networks suffered from a rearrangement of dislocations and, thus, were prone to cyclic softening and local microstructure instability. However, in the HCF regime rearrangement of dislocations was found to be not as pronounced as (local) plasticity was minimized due to the fairly low loading level. Thus, even non-optimized microstructures obtained by ECAP routes characterized by a relatively low number of passes showed good fatigue properties under these loading conditions. These findings are absolutely in line with the results obtained by Bruder already mentioned earlier.^[33]

The fraction of LAGBs characterized by misorientation angles lower than 15° in the EBM-processed cp-Fe is two times higher than the fraction of HAGBs, whereas in the HR Fe the presence of HAGBs dominates the microstructure (cf., Figure 5). However, the total (sub-)boundary line length has to be taken into account for evaluation of properties in the HCF regime: Although the grain boundaries in the EBM-processed cp-Fe are mainly of low-angle character, the total length of grain boundary lines (including all misorientations higher than 2°) related to

the scanned surface, as determined by the OIM software, is two times higher as compared to the HR reference. Based on these observations, a reasonable explanation for the higher fatigue resistance of the EBM-processed cp-Fe (as compared to its HR counterpart) arises. In the HR Fe, the HAGB character and the large grain sizes dominate the microstructure, the hardness, and, thus, the fatigue properties of this material condition. All these relatively coarse features lead to inferior resistance against structural fatigue. Niendorf et al.^[44] focused on the impact of recovery heat treatments in case of UFG IF steel (and related consequences on the LCF performance). In the ECAP condition, a higher hardness (in between 190 and 220 HV1, depending on the ECAP route considered) leads to an improved fatigue performance, being traced back to the finer microstructure. An adequate heat treatment leading to homogeneous recovery and evolution of a balanced mixture of LAGBs and HAGBs even further improves cyclic stability with respect to the given loading conditions. Depending on the heat treatment parameters applied, the microstructural evolution was shown to be different, in some cases even leading to premature failure. This was attributed to the evolution of a detrimental microstructure featuring a coarse-grained microstructure dominated by HAGBs without any remaining substructures and LAGBs, respectively. Consequently, this resulted in a decrease of hardness to 75 HV1 as well as in inferior fatigue strength.^[44] In the present study, the EBM-processed cp-Fe can be directly compared to an UFG IF steel condition characterized by a relatively low number of passes, that is, a microstructure dominated by LAGBs. The high build plate temperatures as well as the thermal history characteristic for the EBM process most probably lead to an in-process recovery treatment, resulting in a homogeneous and fine-grained microstructure with an increased boundary length per area (including HAGBs and LAGBs). In line with results stemming from ECAP-processed material, the fatigue performance is drastically increased in the HCF regime. Obviously, the microstructure shows quite good thermal stability and negligible recrystallization despite EBM processing at elevated temperature (Figure 4). In this regard, the microstructure of the EBM-processed cp-Fe presented herein is similar to that of the UFG IF steel upon non-optimized ECAP route processing,^[44] again underlining the stability of the substructures. Furthermore, according to Bruder's investigations,^[33] LAGBs do not suffer instability in stress-controlled HCF tests, eventually not affecting cyclic stability detrimentally. The increase of yield strength induced by grain refinement, thus, dominates the material behavior. For further in-depth understanding of microstructure evolution, post-mortem EBSD analysis has to be performed in future studies to quantitatively analyze the development of (sub-)grain structures in EBM-processed cp-Fe. Furthermore, the driving forces and elementary mechanisms leading to a specific grain morphology and texture in the EBM process are not fully understood and have to be additionally addressed in future studies. Given the fact that a higher fatigue resistance in the HCF regime and also higher yield strength of the EBM-processed cp-Fe is revealed, investigations in the LCF regime will further shed light on the stability of the LAGBs established by the intrinsic heat treatment being characteristic for the EBM process. Finally, as the intended field of application is implant surgery, the fatigue behavior of EBM-processed cp-Fe in corrosive media will be studied.

4. Conclusion

In present work, EBM-processed cp-Fe samples were studied featuring a very low defect density (cracks as well as pores). Microstructure analysis of the as-built EBM-processed cp-Fe revealed the presence of grains with a relatively high aspect ratio and a high density of LAGBs. According to the literature, these subgrains can be traced back to recovery and grain refinement mechanisms as a result of multiple phase transformations. Direct comparison of the EBM-processed cp-Fe with the HR reference material revealed differences in hardness and strength. Most importantly, the fatigue resistance at 5×10^6 cycles is ≈ 100 MPa higher for the EBM-processed material. This is mainly attributed to a very high fraction of LAGBs and their positive effect on fatigue properties in the HCF regime. With respect to reference conditions taken from the literature, the fatigue resistance of the EBM-processed cp-Fe is between the values of the HR Fe and UFG Fe processed by ECAP.

Acknowledgements

This work was supported by the Deutsche Forschungsgemeinschaft (DFG) under grant number 413259151. The authors acknowledge access to DESY (Hamburg, Germany), a member of the Helmholtz Association HGF. Parts of this research were conducted at PETRA III. The authors gratefully acknowledge experimental support by N. Schell and A. Stark at P07 EH1. Open access funding enabled and organized by Projekt DEAL.

Conflict of Interest

The authors declare no conflict of interest.

Data Availability Statement

Research data are not shared.

Keywords

additive manufacturing, fatigue, microstructure, pure iron, rotating bending

Received: January 7, 2021
Revised: February 18, 2021
Published online: March 10, 2021

- [1] W. S. W. Harun, M. S. I. N. Kamariah, N. Muhamad, S. A. C. Ghani, F. Ahmad, Z. Mohamed, *Powder Technol.* **2018**, 327, 128.
- [2] J. Günther, F. Brenne, M. Droste, M. Wendler, O. Volkova, H. Biermann, T. Niendorf, *Sci. Rep.* **2018**, 8, 1298.
- [3] T. Niendorf, F. Brenne, M. Schaper, A. Riemer, S. Leuders, W. Reimche, D. Schwarze, H. J. Maier, *Rapid Prototyping J.* **2016**, 22, 630.
- [4] F. Yan, W. Xiong, E. Faierman, *Materials* **2017**, 10, 1260.
- [5] C. Körner, H. Helmer, *MATEC Web Conf.* **2014**, 14, 8001.
- [6] H. Helmer, *Mater. Sci. Eng., A* **2016**, 668, 180.
- [7] R. R. Dehoff, M. M. Kirka, W. J. Sames, H. Bilheux, A. S. Tremsin, L. E. Lowe, S. S. Babu, *Mater. Sci. Technol.* **2015**, 31, 931.
- [8] L. E. Murr, *J. Mech. Behav. Biomed. Mater.* **2017**, 76, 164.

- [9] T. Schouman, M. Schmitt, C. Adam, G. Dubois, P. Rouch, *J. Mech. Behav. Biomed. Mater.* **2016**, *59*, 484.
- [10] F. A. Shah, O. Omar, F. Suska, A. Snis, A. Matic, L. Emanuelsson, B. Norlindh, J. Lausmaa, P. Thomsen, A. Palmquist, *Acta Biomater.* **2016**, *36*, 296.
- [11] J. Wieding, T. Lindner, P. Bergschmidt, R. Bader, *Biomaterials* **2015**, *46*, 35.
- [12] P. Fromme, G. W. Blunn, W. J. Aston, T. Abdoola, J. Koris, M. J. Coathup, *Med. Eng. Phys.* **2017**, *41*, 19.
- [13] S. M. Ahmadi, R. Hedayati, Y. Li, K. Lietaert, N. Tümer, A. Fatemi, C. D. Rans, B. Poursan, H. Weinans, A. A. Zadpoor, *Acta Biomater.* **2018**, *65*, 292.
- [14] J. Zhu, Q. Zeng, T. Fu, *Corros. Rev.* **2019**, *37*, 539.
- [15] Y. Li, H. Jahr, K. Lietaert, P. Pavanram, A. Yilmaz, L. I. Fockaert, M. A. Leeftang, B. Poursan, Y. Gonzalez-Garcia, H. Weinans, J. M. C. Mol, J. Zhou, A. A. Zadpoor, *Acta Biomater.* **2018**, *77*, 380.
- [16] Y. Li, K. Lietaert, W. Li, X.-Y. Zhang, M. A. Leeftang, J. Zhou, A. A. Zadpoor, *Corros. Sci.* **2019**, *156*, 106.
- [17] M. Montani, A. G. Demir, E. Mostaed, M. Vedani, B. Previtali, *Rapid Prototyping J.* **2017**, *23*, 514.
- [18] P. Sharma, P. M. Pandey, *Mater. Sci. Eng., C* **2019**, *99*, 838.
- [19] R. Waksman, R. Pakala, R. Baffour, R. Seabron, D. Hellinga, F. O. Tio, *J. Interventional Cardiol.* **2008**, *21*, 15.
- [20] M. Peuster, C. Hesse, T. Schloo, C. Fink, P. Beerbaum, C. von Schnakenburg, *Biomaterials* **2006**, *27*, 4955.
- [21] T. Kraus, F. Moszner, S. Fischerauer, M. Fiedler, E. Martinelli, J. Eichler, F. Witte, E. Willbold, M. Schinhammer, M. Meischel, P. J. Uggowitzer, J. F. Löffler, A. Weinberg, *Acta Biomater.* **2014**, *10*, 3346.
- [22] P. Lejček, M. Roudnická, J. Čapek, D. Dvorský, J. Drahoukoupil, D. Šimek, J. Čížek, P. Svora, O. Molnářová, D. Vojtěch, *Mater. Charact.* **2019**, *154*, 222.
- [23] B. Song, S. Dong, S. Deng, H. Liao, C. Coddet, *Opt. Laser Technol.* **2014**, *56*, 451.
- [24] L. E. Murr, E. Martinez, X. Pan, C. Meng, J. Yang, S. Li, F. Yang, Q. Xu, J. Hernandez, W. Zhu, S. M. Gaytan, F. Medina, R. B. Wicker, *J. Mater. Res. Technol.* **2013**, *2*, 376.
- [25] F. Bachmann, R. Hielscher, H. Schaeben, *Solid State Phenom.* **2010**, *160*, 63.
- [26] N. Schell, A. King, F. Beckmann, T. Fischer, M. Müller, A. Schreyer, *MSF* **2013**, *772*, 57.
- [27] M. Droste, J. Günther, D. Kotzem, F. Walther, T. Niendorf, H. Biermann, *Int. J. Fatigue* **2018**, *114*, 262.
- [28] S. Tammas-Williams, H. Zhao, F. Léonard, F. Derguti, I. Todd, P. B. Prangnell, *Mater. Charact.* **2015**, *102*, 47.
- [29] S. M. Gaytan, L. E. Murr, F. Medina, E. Martinez, M. I. Lopez, R. B. Wicker, *Mater. Technol.* **2009**, *24*, 180.
- [30] G. Chen, Q. Zhou, S. Y. Zhao, J. O. Yin, P. Tan, Z. F. Li, Y. Ge, J. Wang, H. P. Tang, *Powder Technol.* **2018**, *330*, 425.
- [31] N. Hansen, *Scr. Mater.* **2004**, *51*, 801.
- [32] T. Niendorf, F. Rubitschek, H. J. Maier, D. Canadinc, I. Karaman, *J. Mater. Sci.* **2010**, *45*, 4813.
- [33] E. Bruder, *Metals* **2018**, *8*, 191.
- [34] J. A. Muñoz, O. F. Higuera, J. A. Benito, D. Bradai, T. Khelfa, R. E. Bolmaro, A. M. Jorge, J. M. Cabrera, *Mater. Sci. Eng.: A* **2019**, *740–741*, 108.
- [35] Y. Liu, F. Sommer, E. J. Mittemeijer, *Metall. Mater. Trans. A* **2008**, *39*, 2306.
- [36] S. J. Song, F. Liu, Z. H. Zhang, *Acta Mater.* **2014**, *64*, 266.
- [37] *Schmelze, Erstarrung, Grenzflächen: Eine Einführung in die Physik und Technologie flüssiger und fester Metalle* (Eds: P. R. Sahn, I. Egry, T. Volkman), Springer Berlin Heidelberg, Berlin, Heidelberg **1999**.
- [38] N. Raghavan, R. Dehoff, S. Pannala, S. Simunovic, M. Kirka, J. Turner, N. Carlson, S. S. Babu, *Acta Mater.* **2016**, *112*, 303.
- [39] N. Raghavan, S. Simunovic, R. Dehoff, A. Plotkowski, J. Turner, M. Kirka, S. Babu, *Acta Mater.* **2017**, *140*, 375.
- [40] T. Niendorf, D. Canadinc, H. J. Maier, I. Karaman, *Metall. Mater. Trans. A* **2007**, *38*, 1946.
- [41] J. W. Pegues, M. D. Roach, N. Shamsaei, *Mater. Res. Lett.* **2020**, *8*, 8.
- [42] X. He, T. Wang, X. Wang, W. Zhan, Y. Li, *Chin. J. Aeronautics* **2018**, *31*, 2124.
- [43] A. Vinogradov, S. Hashimoto, *Mater. Trans.* **2001**, *42*, 74.
- [44] T. Niendorf, D. Canadinc, H. J. Maier, I. Karaman, *Int. J. Fatigue* **2008**, *30*, 426.
- [45] T. Niendorf, D. Canadinc, H. J. Maier, *Adv. Eng. Mater.* **2011**, *13*, 275.
- [46] T. Niendorf, J. Dadda, D. Canadinc, H. J. Maier, I. Karaman, *Mater. Sci. Eng., A* **2009**, *517*, 225.
- [47] T. Niendorf, H. J. Maier, D. Canadinc, I. Karaman, *Mater. Sci. Eng., A* **2009**, *503*, 160.
- [48] T. Niendorf, D. Canadinc, H. J. Maier, I. Karaman, S. G. Sutter, *IJMR* **2006**, *97*, 1328.